Available online at www.sciencedirect.com
jmr&t
Journal of Materials Research and Technology
https://www.journals.elsevier.com/journal-of-materials-research-and-technology

Original Article

Synthesis and characterization of bubble wrap-like hollow barium silicate–carbonate nanospheres for the epoxidation of styrene

Kok-Hou Tan[a], *Anwar Iqbal*[a,b,*], *Farook Adam*[a], *N.H.H. Abu Bakar*[a],
Rahimi M. Yusop[b], *Mohammad Norazmi Ahmad*[c]

[a] *School of Chemical Sciences, Universiti Sains Malaysia, 11800 Penang, Malaysia*
[b] *School of Chemical Sciences and Food Technology, Faculty of Science and Technology, Universiti Kebangsaan Malaysia, 43600 UKM, Bangi, Malaysia*
[c] *Experimental and Theoretical Research Lab, Department of Chemistry, Kulliyyah of Science, International Islamic University Malaysia, Bandar Indera Mahkota, 25200 Kuantan, Pahang, Malaysia*

ARTICLE INFO

Article history:
Received 5 May 2020
Accepted 30 July 2020

Keywords:
Barium silicate
Barium carbonate
Mesoporous silica
Hollow nanospheres
Alkene epoxidation

ABSTRACT

Novel porous bubble wrap-like hollow barium silicate–carbonate nanospheres were successfully prepared at a barium/CTAB molar ratio of 0.75 and 1.00. The average pore size, BET surface area and total pore volume of the most catalytically active catalyst in the epoxidation of styrene, 1.00BaMST were 5.0 nm, 42 $m^2\ g^{-1}$ and 0.0771 $cm^3\ g^{-1}$, respectively. The styrene epoxidation reaction was carried out using H_2O_2 as an oxidant. Barium silicate and carbonate groups detected on the catalyst's surface are proposed to activate the H_2O_2 and selectively oxidize the styrene to styrene oxide. The 1.00BaMST achieved 63.3% of styrene conversion and 77.8% of epoxide selectivity at mild conditions (3 h, 60 °C). The reaction energy barrier was calculated to be 17.3 kJ mol^{-1}.

1. Introduction

Mesoporous silicas, which comprise of nanopores in the range of 2−50 nm, have received much attention since the discovery of MCM-41 by Kresge and co-workers from Mobil Corporation in 1992 [1]. In contrast to zeolite, which suffered from mass transport limitation, relatively small internal space and small pore openings that are inaccessible to large molecules, mesoporous silicas possess low density, high chemical stability, low dielectric constant, and high thermal resistance. The later has been used in various applications such as catalysis, adsorption, and drug delivery [2,3]. However, due to their weakly acidic nature, pure mesoporous silicas are ineffective in catalytic reactions [4]. Surface modification of the mesoporous silicas with organic or inorganic entities are common strategies to introduce desired catalytic properties for targeted applications [5,6]. Incorporation of metals can be done *via* wet impregnation, vapour deposition, ion-exchange and, direct

---

* *Corresponding author.*
E-mail: anwariqbal@usm.my (A. Iqbal).

https://doi.org/10.1016/j.jmrt.2020.07.109

synthesis [7–9]. Unlike the other methods, uniform metal distribution on the mesoporous silica surface can be achieved at ease by using direct one-pot synthesis [8].

Direct one-pot synthesis has been applied to produce catalysts for selective alkene epoxidation. Cui et al. studied the catalytic potential of a series of one-pot synthesized transition metals (Fe, Ti, Ni, Mn, Sn and Co) supported SBA-15 in styrene epoxidation reaction [10]. Their results showed that the prepared catalysts have a comparable surface area, pore volume and pore diameter regardless of their Si/metal ratio. Among the catalysts, Co incorporated SBA-15 outperformed by achieving a conversion rate of 94.1% and epoxide selectivity up to 65.5%. Rahman and colleagues reported that 24.7% of styrene conversion with 57.0% of styrene oxide selectivity can be obtained by using TUD-1 supported indium oxide catalyst [11]. Li et al. demonstrated that 43.5% of styrene conversion and 86.6% styrene oxide selectivity can be achieved using Cu-KIT-6 catalyst synthesized at pH 3.78 [12]. At this pH, the pore structure of KIT-6 is well-defined and crystalline CuO was absent. The poor performance of Cu-KIT-6 at pH < 3.78 is attributed to the low copper content, while the formation of crystalline CuO at pH > 3.78 is responsible for the lower styrene conversion and epoxide selectivity.

Alkaline earth metals have been added as promoters to boost the reactivity of catalysts in the oxidation of styrene. Sebastian et al. reported that alkaline earth metals (Mg, Ca, Sr and Ba) are better promoters than alkali metals (Na, K, Rb and Cs) when ion-exchanged with sodium cation in zeolite X for epoxidation of styrene with molecular oxygen [13]. The enhanced reactivity is due to the high basicity of the framework oxygen of alkaline earth metal cations, which stabilizes the peroxyl radicals in the zeolite pores. The stability of the radicals was also improved by the strong interaction between the oxygen of the radicals and the alkaline earth metal cations.

Alkaline earth metal oxides have been proven catalytically active in the styrene epoxidation reaction. Choudhary and co-workers reported that barium oxide can convert 40.7% of styrene with up to 78.7% of epoxide selectivity using THBP as oxidant [14]. However, its performance was poorer when impregnated on MCM-41. The decrease in catalytic activity is associated with the lower basicity of the catalyst. Styrene epoxidation using MgO and CaO as catalysts have been recently reported by Bian and Gu [15,16]. The achieved epoxide yields were 85.7% and 96.7%, respectively. Both experiments used hydrogen peroxide as oxidant and acetonitrile as solvent.

In this work, the morphogenesis of bubble wrap-like hollow barium silicate–carbonate nanospheres was systematically studied. The nanospheres were synthesized *via* a one-pot synthesis approach by varying the Ba/surface directing agent (CTAB) molar ratio. Instead of using commercially available silicate precursors such as tetraethylortosilicate (TEOS), rice husk ash was used in this research. To the best of our knowledge, the morphogenesis of bubble wrap-like hollow barium silicate–carbonate nanospheres synthesis using rice husk ash was not discussed in the literature. The catalytic potential of the nanospheres was tested using the styrene epoxidation reaction with H_2O_2 acts as an oxidant. The possible reaction mechanisms and kinetics were determined from the catalytic data and physicochemical properties of the nanospheres.

2. Methods

2.1. *Synthesis of mesoporous barium silicate–carbonate nanospheres*

Sodium silicate solution was first prepared by mixing 3.0 g of rice husk ash (RHA) in 100 mL of 0.8 M NaOH solution. The RHA was produced based on the method of Iqbal et al. [17]. Barium containing structure-directing agent (SDA) solution was made up by dissolving 2.9 g of cetyltrimethylammonium bromide (CTAB) (Sigma-Aldrich, 96%) in 50 mL of distilled water at room temperature. Into this solution, desired mass of $Ba(NO_3)_2$ was then added. The barium containing CTAB solution was added into the sodium silicate solution and stirred at 80 °C for 5 min to achieve a Ba/CTAB molar ratio of 0.25, 0.50, 0.75 and 1.00. Subsequently, the pH of the reactant mixture was adjusted to pH 10 with 2 M HNO_3 and allowed to further react at 80 °C for 6 days. Solid product was filtered, washed with distilled water and dried in the oven at 100 °C for overnight. The dried solid was calcined at 550 °C for 5 h at 1 °C min^{-1} ramp rate. The barium silicate–carbonate nanospheres obtained were labelled as xBaMST where x = Ba/CTAB molar ratio.

2.2. *Catalyst characterization*

The structures of the BaMST catalysts were investigated using powder X-ray diffraction analysis (Bruker D8 Advance, Cu Kα radiation, λ = 1.5418 Å, 0.02°/step, 1 s/step, voltage = 40 kV, current = 40 mA and 0.1 mm Ni β filter) at small (1–10°) and wide-angle (10–90°) range. Scherrer equation (Eq. (1)) was used to estimate the crystallite size of the crystalline phase.

$$d_{XRD} = \frac{K\lambda}{\beta\cos\theta} \tag{1}$$

where d_{XRD} is the crystallite size, K is a shape factor with the value of 0.9 while λ is the wavelength of incident X-ray generated by Cu anode, which equals to 1.5418 Å. β is the full-width at half maximum (FWHM) of the specified diffraction peak while θ represents its Bragg's angle. Both β and θ are in the unit of radian.

Nitrogen adsorption-desorption isotherms were measured at 77 K using Micromeritics ASAP 2020 porosimeter. The pore size distribution was determined using the Barrett, Joyner, and Halenda (BJH) method whereas the surface area was calculated using the Brunauer–Emmett–Teller (BET) equation. Scanning electron microscopy (SEM, QUANTA FEG 650) and transmission electron microscopy (TEM, Phillips CM12 microscope) were used to observe the texture and morphology of the BaMST catalysts. Digimizer version 4.6.1 was used to measure the particle size of BaMST nanoparticles from TEM images. The contrast and the brightness of the images were enhanced using ImageJ software. Inductive coupled plasma-optical emission spectroscopy (ICP-OES, Perkin Elmer OPTIMA 8000) was used to measure the total barium content of the catalyst. The X-ray photoelectron spectroscopy (High-Resolution Multi Technique X-Ray Spectrometer, Axis Ultra DLD XPS, Kratos, Al Kα = 1486.7 eV, Monochromator, calibrated with adventitious carbon at C 1s 284.8 eV) and FT-IR spectroscopy (Perkin Elmer 2000, resolution = 4 cm^{-1}, scan range = 400-4000 cm^{-1}, number of scans = 16) were employed to identify the chemical environment in the catalysts in term of individual elements and functional groups, respectively.

2.3. *Catalytic testing*

The catalytic activity of mesoporous barium silicate catalysts was evaluated using liquid phase styrene epoxidation as a model reaction. 10 mL of acetonitrile (Fisher Scientific) was dispensed into a round bottom flask and mixed with 10 mmol of styrene (98%, Merck). Desired amount of catalyst was introduced to this mixture. After being stirred for 10 min at 80 °C, hydrogen peroxide (QRec, 30–32%) was then added to the mixture under continuous stirring to initiate the reaction. Sample aliquots were withdrawn at a pre-determined time interval and filtered with 0.2 μm syringe membrane filter to halt the reaction. *p*-Xylene was added as an internal standard. GC-FID analysis (Perkin Elmer Clarus 600 Gas Chromatography equipped with Flame Ionization Detector, Inlet temperature: 240 °C; Detector temperature: 240 °C; Carrier gas: compressed air; Flow rate: 20 mL min^{-1}; Programme: 80–240 °C; Ramp rate: 5 °C min^{-1}; Elite-5 column) was used to determine the conversion rate of styrene and epoxidation product selectivity. Reusability test was conducted by regenerating the exhausted catalyst through calcination at 550 °C for 5 h at a 1 °C min^{-1} ramp rate. The catalyst was reused for up to four times through recalcining the exhausted catalyst at 550 °C for 5 h with the ramp rate of 1 °C min^{-1}.

3. Results and discussion

3.1. *Catalyst characterization*

3.1.1. *Elemental analysis*

The total and surface concentrations of Ba measured using XPS and ICP-OES analyses, are given in Fig. 1. As expected, both XPS and ICP-OES indicated an increase in Ba concentration as the Ba/CTAB molar ratio increased. However, the surface Ba concentration is always lower than the total Ba concentration, which suggests that a higher portion of Ba cations was incorporated into the framework of catalysts.

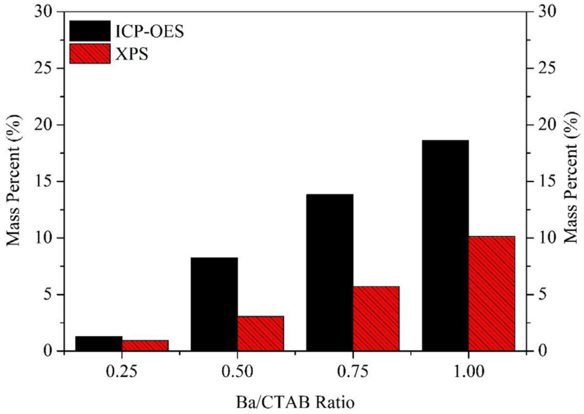

Fig. 1 – The concentration of barium cations in the samples measured by ICP-OES and XPS.

3.1.2. *Structural and morphological analyses*

The small and wide-angle XRD diffractograms of the catalysts are shown in Fig. 2. The absence of any diffraction peaks in the small-angle XRD pattern of 0.25BaMST, 0.50BaMST, and 0.75BaMST indicate that the catalysts did not have any ordered pore arrangements (Fig. 2(a)) [18]. A weak diffraction peak observed at 2.09° for 1.00BaMST indicates the presence of a distinct ordered mesopore structure [19].

The wide-angle XRD diffraction patterns (Fig. 2(b)) indicate that each of the catalysts possesses a different extent of the amorphous phase. A single broad peak at 2θ = ∼22° observable in the wide-angle XRD diffractogram of 0.25BaMST is due to the amorphous nature of the silica framework [20]. Upon increasing the Ba/CTAB molar ratio beyond 0.25, diffraction peaks that attributed to the crystalline barium species started to appear. The diffraction peaks at 2θ = 19.3°, 23.9°, 27.6°, 34.2° and peaks between 40–47° matched the diffraction profile of witherite, an orthorhombic $BaCO_3$ phase [21]. The intensity of the diffraction peak at 2θ = 23.9° in the diffractogram of 1.00BaMST was weaker compared to 0.50BaMST and 0.75BaMST. The observation is attributed to the smaller extent of witherite crystallization in 1.00BaMST. The witherite crystallite size was reduced from 28.3 nm to 3.0 nm when the ratio

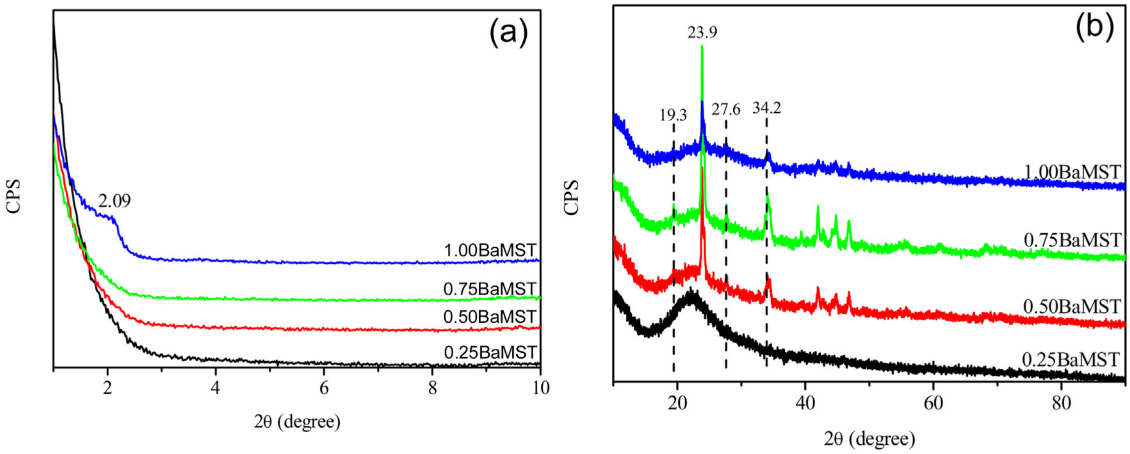

Fig. 2 – The (a) small and (b) wide angle XRD diffractograms of 0.25, 0.50, 0.75 and, 1.00BaMST.

Table 1 – The XRD diffraction data of the catalysts.

Sample	hkl	2θ (degree)	FHWM (radian)	d_{XRD} (nm)[a]
0.25BaMST	–	–	–	–
0.50BaMST	130	34.53	0.003863	28.3
	221	42.00	0.007792	
0.75BaMST	130	34.52	0.008754	16.1
	221	41.99	0.009529	
1.00BaMST	130	34.44	0.048004	3.0
	221	42.09	0.049201	

[a] Crystallite size (d_{XRD}) of witherite phase determined using the Scherrer equation.

Table 2 – The N_2 sorption surface analysis parameters for 0.25BaMST, 0.50BaMST, 0.75BaMST and 1.00BaMST.

Sample	Pore diameter, d_p (nm)	S_{BET} ($m^2\ g^{-1}$)	V_{total} ($cm^3\ g^{-1}$)
0.25BaMST	5.1	204	0.3934
0.50BaMST	7.0	135	0.3342
0.75BaMST	6.6	148	0.3401
1.00BaMST	5.0	42	0.0771

Table 3 – The binding Energy of $Ba3d_{5/2}$, Si2p, O1s and C1s of prepared BaMST.

Sample	Binding energy (eV)				
	Ba		Si2p	O1s	C1s
	$3d_{3/2}$	$3d_{5/2}$			
0.25BaMST	795.9	780.6	103.1	529.5	284.8
			103.7	532.4	
				533.3	
0.50BaMST	795.6	780.4	103.2	529.9	284.8
			103.8	532.5	288.1
				533.3	
0.75BaMST	795.4	780.2	103.2	530.1	284.8
			103.6	532.5	289.0
				533.3	
1.00BaMST	795.4	780.2	103.2	530.2	284.8
			103.7	532.6	289.4
				533.7	

was increased. The XRD parameters of (hkl), angle diffraction, FHWM values, and crystallite size (d_{XRD}) are given in Table 1.

The nitrogen adsorption-desorption isotherms of the BaMST catalysts are shown in Fig. S1. The isotherms of the first three catalysts resemble the Type IV isotherm, which is typical for mesoporous materials. Their hysteresis loops were classified as H1 hysteresis, indicating the presence of uniform mesopores [22]. The position of the hysteresis loops at higher partial pressure ($P/P_0 = 0.6–0.9$) demonstrated that the mesopores are large in size [23]. However, 1.00BaMST possesses a hysteresis at the highest P/P_0 due to the presence of interparticle pores [24].

The N_2 sorption surface analysis parameters are listed in Table 2. The BET surface area of the catalysts decreased as the Ba/CTAB molar ratio was increased. A similar trend was observed for the pore volume. The average pore size increased from 5.1 to 7.0 nm when Ba/CTAB molar ratio increased from 0.25 to 0.50. The expanding diameter of the catalyst particles is also visible in their corresponding TEM images (Fig. 3(a) and 3(b)). This could be due to the increasing number of barium cations at the inner core of the CTAB bilayer (Section 3.1.5). The pore size of BaMST began to decline when Ba/CTAB molar ratio was more than 0.5. The barium cations added were consumed to produce more hollow nanospheres, which eventually aggregate to form bulky hollow sphere aggregates. This is consistent with TEM observation, where larger hollow sphere aggregates were detected when Ba/CTAB ratio was increased from 0.50BaMST to 1.00BaMST. The BET surface area dropped drastically from 0.75BaMST and 1.00BaMST, owing to the extensive formation of hollow sphere aggregates. Chen et al. observed similar observations when they synthesized fullerene from soot [25].

3.1.3. *Electron microscopy analysis*

As seen from the TEM image in Fig. 3(a), the 0.25BaMST contain a mixture of hollow nanospheres and nanorods, each with an average size of 112 nm and 58 nm (Table S1) When the number of moles of barium cations equals or surpasses half of the amount of CTAB, the hollow nanospheres grew bigger and joint together to form bulkier nanosphere aggregates, as seen in the TEM images of 0.50BaMST, 0.75BaMST, and 1.00BaMST (Fig. 3(b)–(d)). The average sizes of these nanospheres were 151, 167 and 232 nm, respectively. The bulky nanosphere aggregates contain hollow architectures originating from the individual hollow nanospheres, which resemble bubble wraps.

The SEM micrographs indicated that the surface topography of the catalysts was constructed of rod- and spherical-shaped nanoparticles (Fig. S2) regardless of molar ratio. However, as the Ba/CTAB molar ratio increased, the rod-shape particles became shorter and more spherical. The highly porous nature of the catalysts can be clearly observed from the SEM images.

3.1.4. *Surface functional groups identification*

The binding energy of chemical species on the surface of the catalysts detected using XPS is given in Table 3, whereas the XPS spectra are given in Figs. S3–S6. The peaks for Si2p and O1s of silica framework (Si—OS—i) were detected in all the catalysts at 103.6–103.8 eV and 532.4–532.6 eV [26,27].

When the barium cation was introduced to one-quarter of the amount of CTAB, a distinct $Ba3d_{5/2}$ binding energy was detected at 780.6 eV along with additional Si2p and O1s peaks at 103.1 eV and 529.5 eV, respectively. Thus, barium silicate ion-pair species are proposed to be present on the surface of 0.25BaMST (Fig. 4(a)). This coincides with several studies that investigated the chemical structure of barium in the silicate framework [28–30].

For 0.50BaMST, the binding energy of $Ba3d_{5/2}$ slightly reduced to 780.4 eV due to the presence of bidentate carbonate groups (Fig. 4(b)). The presence of carbonate anion is indicated by the C1s signal at 288.1 eV and O1s signal at 529.9 eV, respectively [31]. The carbonate group act as a bridge connecting two barium cations, each bonded to a silicate group ($\equiv$SiO—$^{-}$). The surface silicate group is represented by Si 2p peak at 103.2 eV [32].

Further increasing Ba/CTAB to 0.75 led to the formation of surface barium carbonate species, which shifted the $Ba3d_{5/2}$

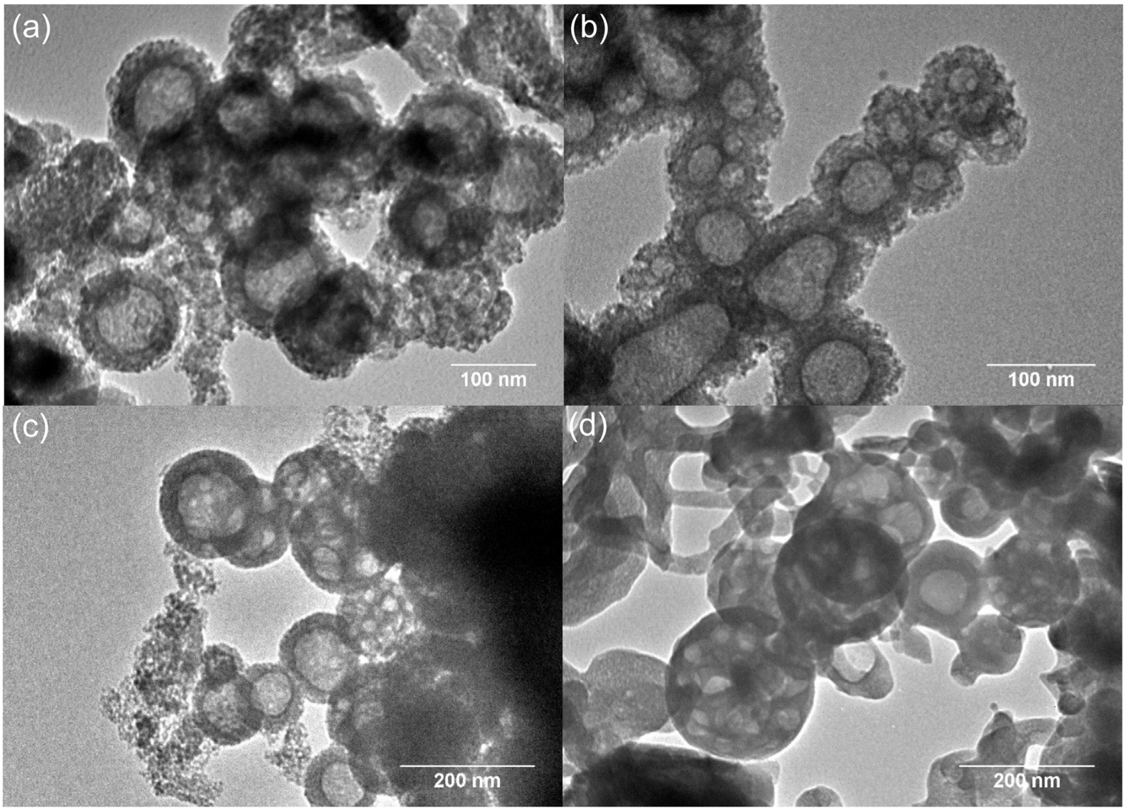

Fig. 3 – The TEM micrograph of (a) 0.25 BaMST, (b) 0.50 BaMST, (c) 0.75 BaMST, and (d) 1.00 BaMST. Scale bar = 100 nm.

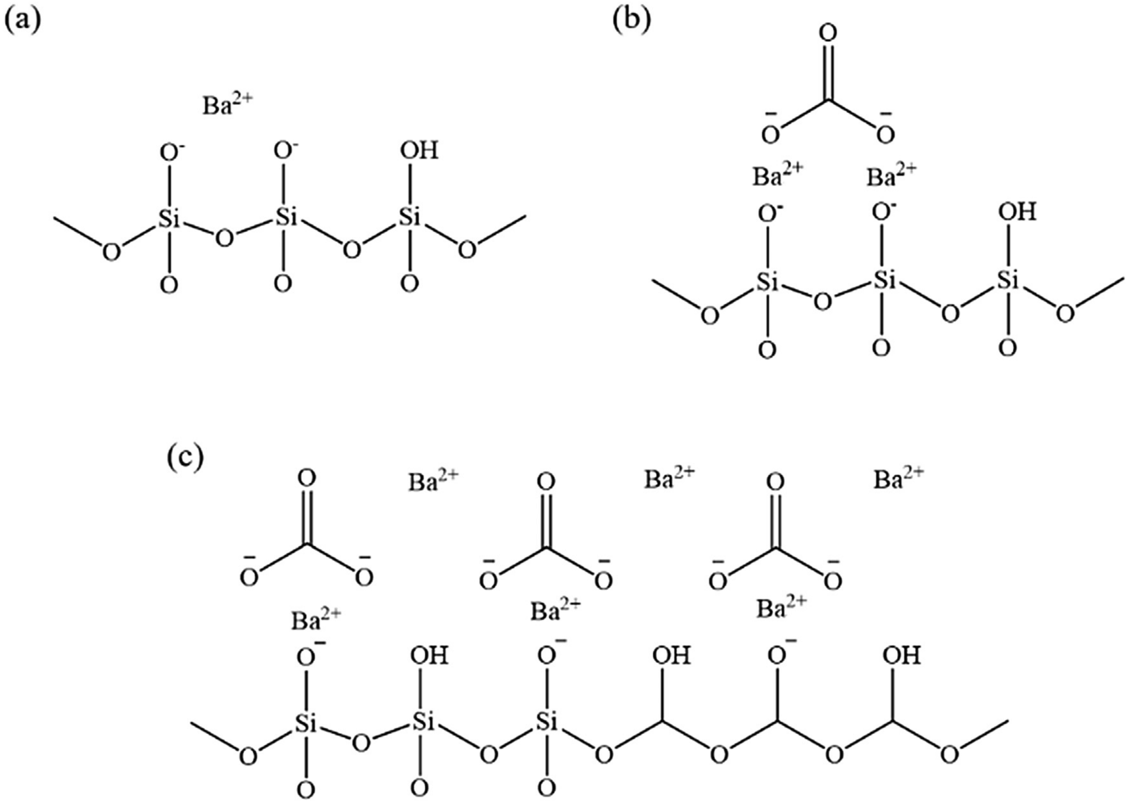

Fig. 4 – The proposed structure of (a) barium silicate, (b) bidentate barium carbonate, and (c) barium carbonate surface active sites.

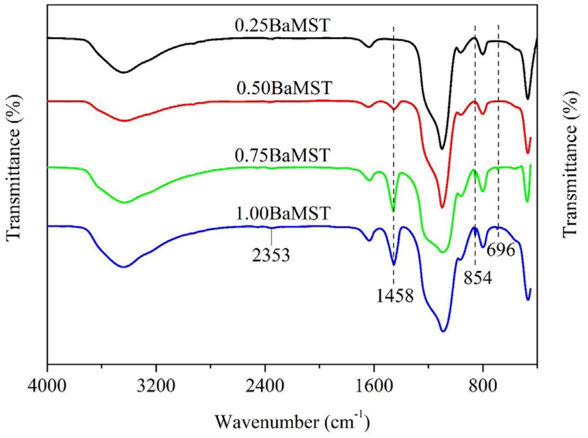

Fig. 5 – The FT-IR spectra of the BaMST catalysts.

to 780.2 eV (Fig. 4(c)) [33]. The existence of the bulk barium carbonate phase was indicated by the O1s and C1s peaks at 530.1 eV and 289.0 eV. A similar carbonate phase was observed in 1.00BaMST. Barium silicate Ba3d$_{5/2}$ peak was absent due to the extensive aggregation of hollow nanospheres, which buries the barium silicate groups inside the bulk hollow nanospheres [34].

The FTIR spectra of the catalysts are shown in Fig. 5. The broad absorption band at 3439 cm^{-1} and medium peak at 1635 cm^{-1} are attributed to the OH— group of water [35]. The peaks located at 1097 and 1228 cm^{-1} correspond to the asymmetric stretching vibration of Si—OS—i, whereas the FTIR band at 802 cm^{-1} is due to the symmetric stretching of Si—OS—i group [36]. The signal at 466 cm^{-1} is due to the bending vibration of SiOS—i [36,37]. The typical vibration of surface silanol groups is evidenced by the signal at 960 cm^{-1} [37,38]. The signal at 854 cm^{-1} is assigned to the bidentate carbonate species [39]. The vibration of the witherite carbonate group has given rise to the IR bands at 1458 cm^{-1} and 2353 cm^{-1} [21,40]. The intensity of these peaks increased as the Ba/CTAB molar ratio was increased. The peak at 696 cm^{-1} corresponds to the metal-oxygen bond [35,41].

3.1.5. *Morphogenesis of the hollow nanospheres*

The possible morphogenesis of the catalysts is illustrated in Scheme 1. The mechanism was proposed based on XPS, XRD, TEM and SEM analyses. Under the synthesis conditions, spherical-shaped, bilayer CTAB micelles containing aqueous environment in its core were formed. Barium hydroxide $Ba(OH)_2$ will be formed when the $Ba(NO_3)_2$ containing CTAB solution was added in the sodium silicate mixture. The barium cations, hydroxide, nitrate and bromide anions will be positioned in the aqueous core. During the gelation process, the silanol group (Si–OH) reacts with the $Ba(OH)_2$ in the aqueous core *via* a condensation reaction, forming a Si—OB—a bond. Since the CTAB micelles acted as a template, the condensation reaction takes place surrounding the hollow spherical-shaped micelles. As a result, spherical-shaped hollow nanoparticles were formed after the template removal.

Layers of witherite were not formed on the surface of 0.25BaMST due to the low concentration of Ba cations. The available Ba cations reacted with silanol groups and transformed to be part of the silica framework. The structure of 0.25BaMST is shown in Scheme 1(a). As the molar ratio of barium cation increased to 0.50, surface Ba cations can react with the CO_2 liberated from the thermal decomposition of CTAB to form layers of witherite on the surface of the catalyst (Scheme 1(b)). When the Ba/CTAB exceeds 0.50, some of the excess Ba cations may react with the surface silanol groups of the neighbouring nanospheres to form bulkier nanospheres (Scheme 1(c)), as observed in the TEM images of 0.75BaMST and 1.00BaMST (Fig. 3(c) and (d)).

Table 4 – The styrene conversion and product selectivities against Ba/CTAB ratio.

Ba/CTAB molar ratio	Conv[a] (%)	Selectivity (%)		
		StO	Bz	PA
0.25	13.8	18.0	74.6	0.8
0.50	12.5	35.1	49.8	12.6
0.75	8.8	36.0	46.7	13.9
1.00	20.1	36.1	44.9	15.5

Reaction conditions: 50 mg catalyst, 10 mmol styrene, 10 mmol H_2O_2, 10 mL acetonitrile, 1 h and 80 °C.

[a] Styrene conversion.

3.2. *Catalytic testing*

The catalytic activity of prepared BaMST catalysts were tested in the styrene epoxidation reaction with H_2O_2 as oxidant. The influences of synthesis precursor Ba/CTAB molar ratio, reactant (styrene:H_2O_2) loading, catalyst loading, and reaction temperature were investigated to obtain the reaction optimum conditions.

3.2.1. *Effect of Ba/CTAB molar ratio*

The conversion rate of styrene was 13.8% when 0.25BaMST was used (Ba/CTAB = 0.25) (Table 4). The products obtained were benzaldehyde (BZ, 74.6%), styrene oxide (StO, 18.0%) and phenylacetaldehyde (PA, 0.8%). The highest styrene conversion (20.1%) and StO selectivity (36.1%) were observed when 1.00BaMST was used. Lower conversion of styrene was observed for 0.50BaMST and 0.75BaMST even though they have similar surface chemistry and larger surface area compared to 1.00BaMST. The pore diameter of 0.50BaMST and 0.75BaMST is in the range of 6–7 nm, whereas the pore diameter of 1.00BaMST was 5 nm. Larger pore size allows the reactants to diffuse in and out from the pores easily compared to pores with smaller sizes. Thus, in larger pores, the interaction rate among the reactants (styrene and H_2O_2) and with the surface active sites will be lower. This explained the lower styrene conversion when 0.50BaMST and 0.75BaMST were used compared to 1.00BaMST.

Reaction mechanisms of the styrene epoxidation catalysed by the catalysts are shown in Fig. 6. The mechanisms are deduced based on the data obtained from XPS analysis, XRD analysis and catalytic data (Table 4). In the presence of a barium silicate component, a Ba–H_2O_2 adduct will be formed when the H_2O_2 interacts with the Ba^{2+} cation (Fig. 6 (a)). The electrophilic addition reaction between the adduct and the styrene side chain will form the intermediate (**A**), which rear-

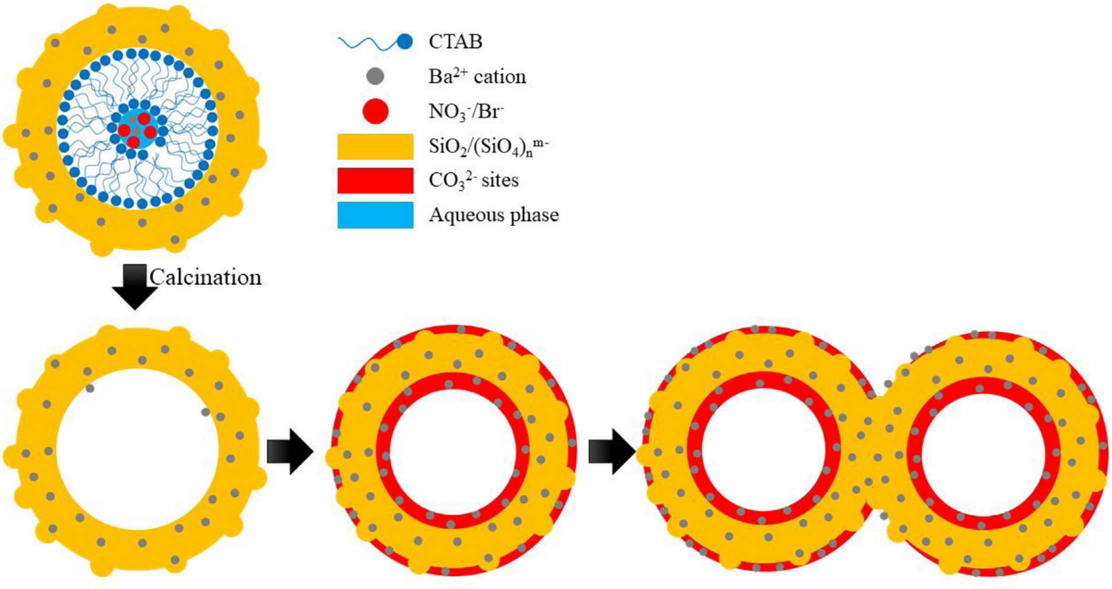

(a) Ba/CTAB=0.25 (b) Ba/CTAB=0.50 (c) Ba/CTAB=0.75, 1.00

Scheme 1 – The relationship between the catalyst's architecture and Ba/CTAB molar ratio of (a) 0.25, (b) 0.50 and (c) above 0.75.

ranges to form StO. The adduct can further react with the StO to form intermediate (**B**). The rearrangement of electrons in the intermediate will produce BZ and formaldehyde. The formaldehyde might have escaped to the atmosphere due to its low boiling point. Thus, it was not detected during the GC and GCMS analysis. In the presence of the carbonate component, hydroxyhydroperoxy species will be formed upon reacting with the H_2O_2 (Fig. 6(b)). This species reacts with the styrene side chain to form carbonate–StO complex (**C**) and water. The StO is released and the carbonate anion is regenerated upon internal electron rearrangement. Due to the steric hindrance and electrostatic repulsion between the oxygenated hydroxyhydroperoxy species and StO, further oxidation of StO to BZ will be suppressed. The reaction mechanisms were proposed based on the catalytic data (Table 4), XRD and XPS analyses. Based on the results, 1.00BaMST with distinct high styrene conversion and high StO selectivity was chosen for the optimization of other parameters.

3.2.2. *Effect of styrene:H_2O_2 ratio*

The influence of the amount of H_2O_2 was investigated by varying the styrene-to-H_2O_2 ratio in the reactant mixture (Table 5). When styrene:H_2O_2 ratio was 1:1, the styrene conversion was less than 10%. The selectivity of StO and BZ was 12.5% and 45.3%, respectively. The data suggested that at 1:1, the self-decomposition rate of H_2O_2 took place at a faster rate compared to the rate of H_2O_2 interaction with the active sites. The self-decomposed products of H_2O_2, such as hydroxyl radicals can cleave the alkene side group of styrene and the epoxide ring, leading to the formation of more BZ.

The styrene conversion doubled and the StO selectivity increased to 36.1% when the styrene:H_2O_2 ratio was increased to 1:2. Further increase in the H_2O_2 concentration resulted in an increase of styrene conversion and changed the product distribution, whereas the selectivity of StO rose to ~50.0% whereas the selectivity of BZ dropped to below 40.0%. The selectivity of PA was slightly higher at 1:4 molar ratio compared to 1:6 and 1:10 molar ratios. Increasing the styrene:H_2O_2 molar ratio beyond 1:6 has shown an increase in styrene conversion but a drop in StO selectivity, which is because of the limited surface-active sites available for activation of H_2O_2.

Table 5 – The styrene conversion and product selectivities against styrene/H_2O_2 ratio.

Styrene/H_2O_2 ratio	Conv[a] (%)	Selectivity (%)		
		StO	Bz	PA
1:1	8.6	12.5	45.3	13.0
1:2	20.1	36.1	44.9	15.5
1:4	38.4	51.0	30.3	17.5
1:6	49.8	50.1	35.0	14.5
1:8	60.2	46.4	36.9	13.3

Reaction conditions: 50 mg 1.00BaMST catalyst, 10 mmol styrene, 10 mL acetonitrile, 1 h and 80 °C.

[a] Styrene conversion.

Due to its higher styrene conversion and comparable StO selectivity, 1:6 molar ratio was used to evaluate other reaction parameters instead of 1:4. The results have proven that the molar ratio of styrene to H_2O_2 can affect the rate of styrene conversion and product distribution.

3.2.3. *Effect of mass of catalyst*

The conversion of styrene increased significantly from 46.4% to 58.7% when the catalyst mass was increased from 25 mg to 100 mg (Table 6). Further increase in catalyst loading beyond 100 mg did not result in any significant change in the conversion rate. The BZ selectivity was reduced while the StO selectivity was increased following this increment. The

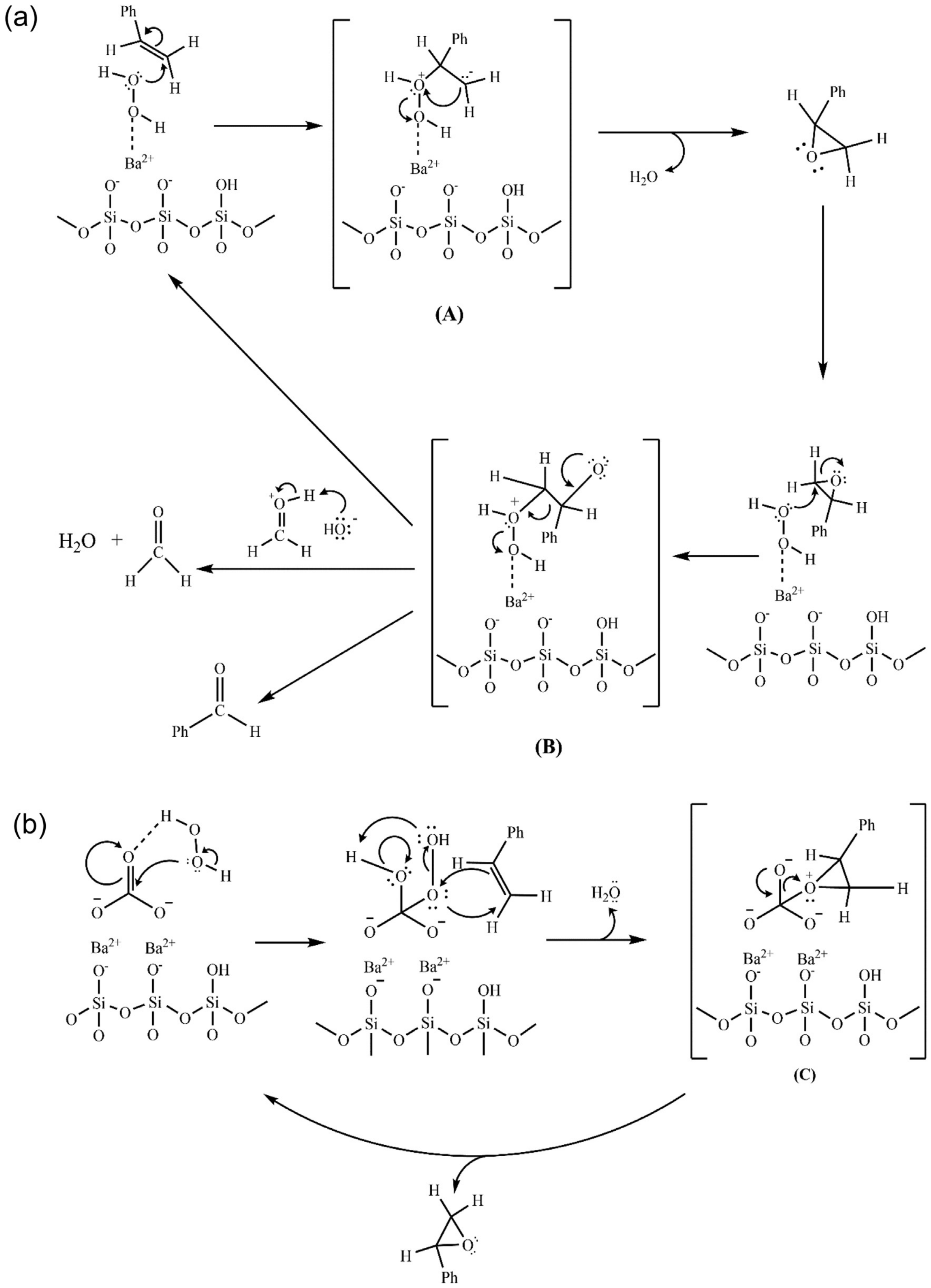

Fig. 6 – The proposed reaction mechanism for the epoxidation of styrene catalysed by (a) barium silicate species and (b) barium carbonate species.

Table 6 – The styrene conversion and product selectivities against the mass of catalyst.

Mass of catalyst (mg)	Conv[a] (%)	Selectivity (%)		
		StO	Bz	PA
25	46.4	51.3	28.5	17.2
50	49.8	50.1	35.0	14.5
75	56.7	63.4	22.5	13.9
100	58.7	67.7	18.0	14.1
125	59.0	71.4	15.5	12.9
150	59.9	69.7	14.1	14.4

Reaction conditions: 1.00BaMST catalyst, 10 mmol styrene, 60 mmol H_2O_2, 10 mL acetonitrile, 1 h and 80 °C.

[a] Styrene conversion.

Table 7 – The styrene conversion and product selectivities against reaction temperature (T).

T (°C)	Conv[a] (%)	Selectivity (%)		
		StO	Bz	PA
40	41.4	70.2	10.8	18.3
60	54.8	74.3	7.7	17.7
80	59.0	71.4	15.5	12.9
100	67.6	62.4	23.1	11.8

Reaction conditions: 125 mg 1.00BaMST catalyst, 10 mmol styrene, 60 mmol H_2O_2, 10 mL acetonitrile and 1 h.

[a] Styrene conversion.

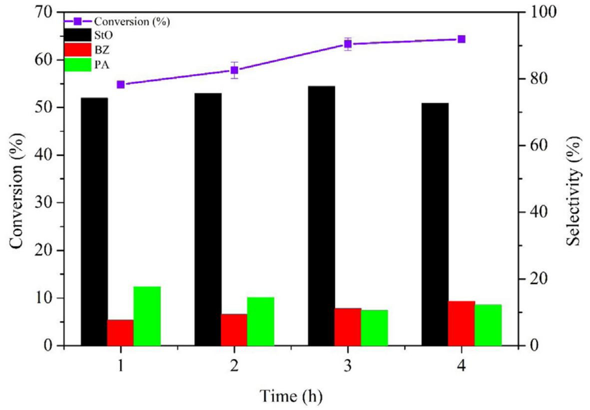

Fig. 7 – The influence of reaction time on the catalytic performance of 1.00BaMST. Reaction conditions: 125 mg of 1.00BaMST catalyst, 10 mmol of styrene, 60 mmol of H_2O_2, 10 mL of acetonitrile, 60 °C, 250 rpm, reflux.

selectivity of BZ was the highest (~25.0%) when 50 mg of catalyst was used while the highest StO selectivity of 71.4% was obtained when 125 mg of 1.00BaMST was used. However, due to mass diffusion limitation, which restricts the interaction between reactants and surface barium cation active sites, the StO selectivity started to drop when the mass was increased beyond 125 mg [42]. The selectivity of PA underwent slight changes when the catalyst mass was varied. Based on the result, 125 mg was identified as the optimum catalyst loading for the liquid phase styrene epoxidation using hydrogen peroxide catalysed by 1.00BaMST.

3.2.4. *Effect of reaction temperature*

Results in Table 7 indicated the dependence of styrene conversion rate and product selectivity on the reaction temperature. It was observed that the conversion increased significantly from 41.4% to 67.6% when the reaction temperature was raised from 40 to 100 °C. The highest StO selectivity (74.3%) was achieved at 60 °C. Further increase in temperature reduced the StO selectivity, which is due to the accelerated self-decomposition of H_2O_2 at the higher temperatures. At temperature beyond 60 °C, higher H_2O_2 self-decomposition and epoxide ring-opening rate led to the rapid oxidation of StO molecules to BZ [43]. The percentage of BZ increased from 7.7% (60 °C) to 23.1% (100 °C), while the selectivity of StO decreased from 74.3% to 62.4%. Due to the better catalytic performance at 60 °C, the kinetics studies were carried out at this temperature.

3.2.5. *Kinetics studies*

Further investigation into the reaction kinetics revealed that about 80% of the styrene epoxidation process occurred at the first one hour of the reaction. As shown in the reaction profile in Fig. 7, both the conversion rate of styrene and epoxide selectivity approached saturation after one hour under optimum conditions. The highest styrene conversion rate and epoxide selectivity of 63.3% and 77.8%, respectively, were achieved at 3 h. Significant changes were not observed when the reaction time reached 4 h.

The experimental data were fitted into various kinetic models to determine the order and rate constant of the studied reaction (Table S2). The pseudo-first-order kinetic model, with the R-square values within 0.9970–0.9987 was selected to determine the rate constant for the Arrhenius plot (Table S2). The rate constant increased from 9.6479×10^{-5} M s^{-1} to 2.9358×10^{-4} M s^{-1} when the temperature was increased from 40 to 100 °C. An Arrhenius plot of ln k against 1/T was then plotted to obtain the activation energy, E_a (Fig. S7). By substituting the value of slope to Arrhenius equation, the activation energy of the reaction was determined to be 17.3 kJ mol^{-1} ($R^2 = 0.9198$). This energy is much lower than the self-decomposition activation energy of hydrogen peroxide of 75 kJ mol^{-1} [44]. Since the catalytic pathway is preferred over the thermal decomposition of H_2O_2, the formation of benzaldehyde was restricted, and the epoxide selectivity was improved.

3.2.6. *Reusability testing*

The conversion of styrene and StO selectivity started to decrease as the catalyst was reused (Fig. 8). At the end of the third reuse, the conversion of styrene was ~37.5%, whereas the StO selectivity dropped to 2.5%. The selectivity of BZ initially increased up to the second reuse and dropped at the end of the third reuse. Surprisingly, the selectivity of PA increased to 87.8% when the catalyst was recycled for the third time. The reduction of carbonate intensity (1456 cm^{-1}) was observed in the FTIR spectrum (Fig. 9) of the spent 1.00BaMST. After repeated heat treatments, the barium carbonate species may have decomposed to barium silicate and CO_2. The transformation of barium carbonate to barium silicate and increases in the number of silanol group may have increased the surface acidity, thus catalysing the isomerization of StO to PA. The

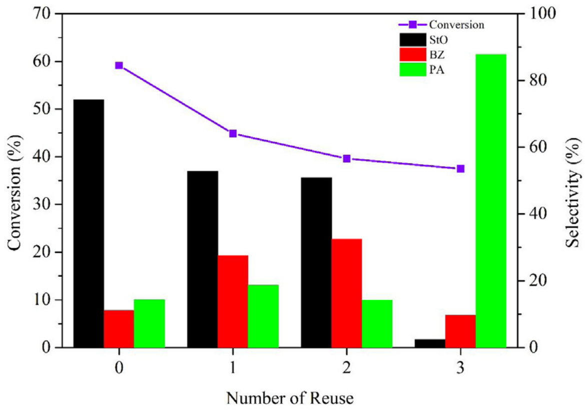

Fig. 8 – The reusability of 1.00BaMST for the first four cycles of epoxidation reaction.

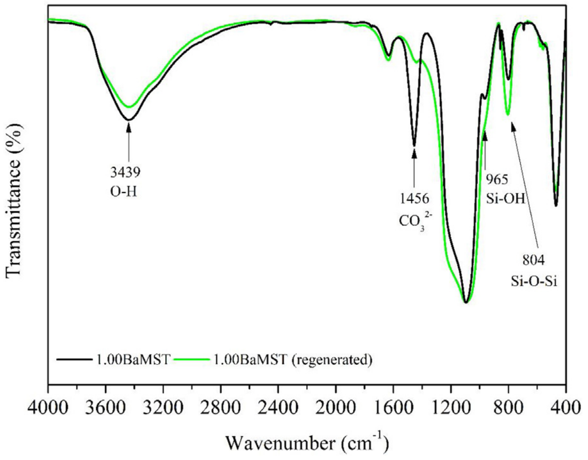

Fig. 9 – The FT-IR spectrum of fresh 1.00BaMST catalyst (black) and regenerated catalyst (green).

observation revealed that 1.00BaMST could serve as an acid catalyst after exhausted in the styrene epoxidation reaction.

4. Conclusion

Novel bubble wrap-like hollow barium silicate–carbonate nanospheres can be prepared by using a barium/CTAB molar ratio of 0.75 and 1.00. At Ba/CTAB molar ratio = 1.0 (1.00BaMST), hollow nanospheres, having an average pore size of 5.0 nm, BET specific area of 42 m^2 g^{-1} and a total pore volume of 0.0771 cm^3 g^{-1}, can be obtained. The surface of the hollow nanospheres contains barium silicates and barium carbonate groups. The catalyst was active in the epoxidation of styrene using H_2O_2 as an oxidant. The highest conversion of styrene (63.3%) and styrene oxide selectivity (77.8%) were achieved when the reaction was carried out at 60 °C for 3 h. It was found that this reaction follows the pseudo-first-order kinetic model. The catalyst reduced the reaction activation energy to 17.3 kJ mol^{-1}, which subsequently improves the rate of reaction while suppressing the self-decomposition of H_2O_2. The catalytic activity of barium silicate–carbonate hollow nanosphere (1.00BaMST) decreased upon the regeneration and eventually transformed into acidic catalyst after three cycles of reuses.

Conflicts of interest

The authors declare no conflicts of interest.

Acknowledgements

The authors would like to acknowledge the financial support from the Ministry of Education Malaysia (Higher Education) through the Fundamental Research Grant Scheme (FRGS) (203/PKIMIA/6711790), Universiti Sains Malaysia Research University Grant (RUI) (1001/PKIMIA/8011083), Universiti Sains Malaysia Short Term Grant (304/PKIMIA/6313215), and Trans-disciplinary Research Grant Scheme (TRGS) (203/PKIMIA/679001). We would also like to thank Geran Universiti Penyelidikan Universiti Kebangsaan Malaysia (GUP-2019-045) which partly supported this work. We would like to extend our gratitude to the RSC Materials Chemistry Division for the financial support given to Mr Kok-Hou Tan through RSC Travel Grant for PhD Students and Early Career Scientists, Ministry of Education Malaysia (Higher Education) and Universiti Sains Malaysia for the Post-Doctoral Training Fellowship awarded to Anwar Iqbal.

Appendix A. Supplementary data

Supplementary material related to this article can be found, in the online version, at doi:https://doi.org/10.1016/j.jmrt.2020.07.109.

REFERENCES

[1] Kresge CT, Leoniwicz ME, Roth WJ, Vartuli JC, Beck JS. Ordered mesoporous molecular sieves synthesized by a liquid-crystal template mechanism. Nature 1992;359:710–2.

[2] Sayari A, Shee D, Al-Yassir N, Yang Y. Catalysis over pore-expanded MCM-41 mesoporous materials. Top Catal 2010;53:154–67, http://dx.doi.org/10.1007/s11244-009-9420-0.

[3] Bhattacharyya S, Lelong G, Saboungi ML. Recent progress in the synthesis and selected applications of MCM-41: a short review. J Exp Nanosci 2006;1:375–95, http://dx.doi.org/10.1080/17458080600812757.

[4] Abdel Salam MS, Betiha MA, Shaban SA, Elsabagh AM, Abd El-Aal RM, Elkady FY. Synthesis and characterization of MCM-41-supported nano zirconia catalysts. Egypt J Pet 2015;24:49–57, http://dx.doi.org/10.1016/j.ejpe.2015.02.005.

[5] Taib NI, Endud S, Katun MN. Functionalization of mesoporous Si-MCM-41 by grafting with trimethylchlorosilane. Int J Chem 2011;3:2–10, http://dx.doi.org/10.5539/ijc.v3n3p2.

[6] Rath D, Parida KM. Copper and nickel modified MCM-41 an efficient catalyst for hydrodehalogenation of chlorobenzene at room temperature. Ind Eng Chem Res 2011;50:2839–49, http://dx.doi.org/10.1021/ie101314f. American Chemical Society.

[7] Köhn R, Fröba M. Nanoparticles of 3d transition metal oxides in mesoporous MCM-48 silica host structures: synthesis and

characterization. Catal Today 2001;68:227–36, http://dx.doi.org/10.1016/S0920-5861(01)00282-6.
[8] Ramanathan A, Subramaniam B. Metal-incorporated mesoporous silicates: tunable catalytic properties and applications. Molecules 2018;23:1–13, http://dx.doi.org/10.3390/molecules23020263.
[9] Tang Q, Zhang Q, Wu H, Wang Y. Epoxidation of styrene with molecular oxygen catalyzed by cobalt(II)-containing molecular sieves. J Catal 2005;230:384–97, http://dx.doi.org/10.1016/j.jcat.2004.12.017.
[10] Cui H, Zhang Y, Qiu Z, Zhao L, Zhu Y. Synthesis and characterization of cobalt-substituted SBA-15 and its high activity in epoxidation of styrene with molecular oxygen. Appl Catal B Environ 2010;101:45–53, http://dx.doi.org/10.1016/j.apcatb.2010.09.003.
[11] Rahman S, Farooqui SA, Rai A, Kumar R, Santra C, Prabhakaran VC, et al. Mesoporous TUD-1 supported indium oxide nanoparticles for epoxidation of styrene using molecular O_2. RSC Adv 2015;5:46850–60, http://dx.doi.org/10.1039/c5ra03400k.
[12] Li B, Luo X, Huang J, Wang X, Liang Z. One-pot synthesis of ordered mesoporous Cu-KIT-6 and its improved catalytic behavior for the epoxidation of styrene: effects of the pH value of the initial gel. Chin J Catal 2017;38:518–28, http://dx.doi.org/10.1016/S1872.
[13] Sebastian J, Jinka KM, Jasra RV. Effect of alkali and alkaline earth metal ions on the catalytic epoxidation of styrene with molecular oxygen using cobalt(II)-exchanged zeolite X. J Catal 2006;244:208–18, http://dx.doi.org/10.1016/j.jcat.2006.09.005.
[14] Choudhary VR, Jha R, Jana P. Epoxidation of styrene by TBHP to styrene oxide using barium oxide as a highly active/selective and reusable solid catalyst. Green Chem 2006;8:689, http://dx.doi.org/10.1039/b604937k.
[15] Bian X, Gu Q, Shi L, Sun Q. Epoxidation of styrene with hydrogen peroxide over MgO catalyst. Chin J Catal 2011;32:682–7, http://dx.doi.org/10.3724/SP.J.1088.2011.01161.
[16] Gu Q, Han D, Shi L, Sun Q. Styrene epoxidation with hydrogen peroxide over calcium oxide catalysts prepared from various precursors. J Nat Gas Chem 2012;21:452–8, http://dx.doi.org/10.1016/S1003-9953(11)60390-3.
[17] Iqbal A, Hou TK, Shaari US, Adam F, Abu Bakar NHH, Wilson LD, et al. Aminolysis of styrene oxide catalyzed by microporous silica with longitudinal and spiral pore channels prepared from rice husk ash. Mater Today Proc 2018;5:21584–93, http://dx.doi.org/10.1016/j.matpr.2018.07.007. Elsevier.
[18] Adam F, Iqbal A. The liquid phase oxidation of styrene with tungsten modified silica as a catalyst. Chem Eng J 2011;171:1379–86, http://dx.doi.org/10.1016/j.cej.2011.05.052.
[19] Huang L, Zhang Q, Dai L, Shen X, Chen W, Cai K. Phenylboronic acid-modified hollow silica nanoparticles for dual-responsive delivery of doxorubicin for targeted tumor therapy. Regen Biomater 2017;4:111–24, http://dx.doi.org/10.1093/rb/rbw045.
[20] Adam F, Iqbal A. The oxidation of styrene by chromium-silica heterogeneous catalyst prepared from rice husk. Chem Eng J 2010;160:742–50, http://dx.doi.org/10.1016/j.cej.2010.04.003.
[21] Yao Q, Guan Y, Zhou G, Fu S. Witherite nanorods form mesocrystals: a direct experimental examination of a dipole-driven self-assembly model. Eur J Miner 2012;24:519–26, http://dx.doi.org/10.1127/0935-1221/2012/0024-2186.
[22] Thommes M, Kaneko K, Neimark AV, Olivier JP, Rodriguez-Reinoso F, Rouquerol J, et al. Physisorption of gases, with special reference to the evaluation of surface area and pore size distribution (IUPAC Technical Report). Pure Appl Chem 2015;87:1051–69, http://dx.doi.org/10.1515/pac-2014-1117.
[23] Yue Y, Fulvio PF, Dai S. Hierarchical metal-organic framework hybrids: perturbation-assisted nanofusion synthesis. Acc Chem Res 2015;48:3044–52, http://dx.doi.org/10.1021/acs.accounts.5b00349.
[24] Lee J, Kim J, Hyeon T. A facile synthesis of bimodal mesoporous silica and its replication for bimodal mesoporous carbon. Chem Commun 2003;3:1138–9, http://dx.doi.org/10.1039/b301535a.
[25] Chen J, Sheng G, Liu S, Liu Z, Liu Z, Fu J. BET surface area and porous structure of fullerenes and fullerene soots. Chem Res Chin Univ 1999;15:90–3.
[26] Thompson CJ, Loring JS, McGrail BP, Rosso KM, Ilton ES, Martin PF, et al. Evidence for carbonate surface complexation during forsterite carbonation in wet supercritical carbon dioxide. Langmuir 2015;31:7533–43, http://dx.doi.org/10.1021/acs.langmuir.5b01052.
[27] Simonsen ME, Sønderby C, Li Z, Søgaard EG. XPS and FT-IR investigation of silicate polymers. J Mater Sci 2009;44:2079–88, http://dx.doi.org/10.1007/s10853-009-3270-9.
[28] Akkopru B. Adsorption of water on silica and silicate glasses. The Pennsylvania State University; 2013.
[29] Sprenger D, Bach H, Meisel W, Gütlich P. XPS study of leached glass surfaces. J Non Cryst Solids 1990;126:111–29, http://dx.doi.org/10.1016/0022-3093(90)91029-Q.
[30] Genevès T, Domenichini B, Imhoff L, Potin V, Heintz O, Peterlé PM, et al. Elaboration and characterization of barium silicate thin films. Micron 2008;39:1145–8, http://dx.doi.org/10.1016/j.micron.2008.05.010.
[31] Ghelamallah M, Fertout RI, Kacimi S. Impact of barium on surface and reactivity of TiO_2. In: Oral AY, Bahsi ZB, Ozer M, editors. Int. Congr. Energy Effic. Energy Relat. Mater. Springer; 2014. p. 199–203.
[32] Celotta R, Lucatorto T. Advances in surface science, vol. 38. San Diego: Academic Press; 2001, http://dx.doi.org/10.1016/S1079-4042(01)80051-5.
[33] Caballero AC, Fernändez JF, Moure C, Durán P, Fierro JLG. Dopant distribution and grain growth control in $BaTiO_3$ ceramics doped with ZnO-SiO_2-P_2O_5. J Eur Ceram Soc 1997;17:1223–30, http://dx.doi.org/10.1016/s0955-2219(96)00230-0.
[34] Liu C, Zhang W, Li H. Selective flotation of apatite from calcite using 2-phosphonobutane-1,2,4-tricarboxylic acid as depressant. Miner Eng 2019;136:62–5, http://dx.doi.org/10.1016/j.mineng.2019.03.003.
[35] Paz GL, Silva F das CM, Araújo MM, Lima F das CA, Luz GE. Structure elucidation of alkaline earth impregnated MCM-41 type mesoporous materials obtained by direct synthesis: an experimental and theoretical study. J Mol Struct 2014;1068:8–13, http://dx.doi.org/10.1016/j.molstruc.2014.03.054.
[36] Deshpande MR, Joshi UD. Coal fly ash based MCM-41 as a solid catalyst in Knoevenagel condensation reaction. Res Dir 2014;1:1–6.
[37] Bajenaru L, Nastase S, Matei C, Berger D. Studies on the synthesis of mesoporous aluminosilicates as carries for drug delivery systems. UPB Sci Bull 2011;73:1–6.
[38] Hamzah Z, Narawi N, Rasid HM, Nazirah A, Yusoff M. Synthesis and characterization of mesoporous material functionalized with different silylating agent and their capability to remove Cu^{2+}. Malaysian J Anal Sci 2012;16:290–6.
[39] Wilkes MF. A catalytic and solid state study of lanthanum doped ceria; 1999.
[40] Chasan DE, Norwitz G. Infrared determination of inorganic sulfates and carbonates by the pellet technique. In: Malaysian J Anal Sci; 1969, 21.

[41] Chen D, Zeng Z, Zeng Y, Zhang F, Wang M. Removal of methylene blue and mechanism on magnetic γ-Fe_2O_3/SiO_2 nanocomposite from aqueous solution. Water Resour Ind 2016;15:1–13, http://dx.doi.org/10.1016/j.wri.2016.05.003.

[42] DeLasa HI, Serrano-Rosales B. Advances in chemical engineering: photocatalytic technologies. Academic; 2009.

[43] Yazici EY, Deveci H. Factors affecting decomposition of hydrogen peroxide. Proc. XIIth Int. Miner. Process. Symp 2010:609–16, http://dx.doi.org/10.13140/RG.2.1.1530.0648.

[44] Moelwyn Hughes EA. The chemical statics and kinetics of solutions. London: Academic Press Inc; 1971.